

Investigation of Phase and Wavelength-induced Errors in Full-Wave Radar Tomography of High Contrast Domain: an Application to Small Solar System Bodies

Yusuf Oluwatoki Yusuf^{a,b}, Astrid Dufaure^b, Liisa-Ida Sorsa^a, Christelle Eyraud^b, Sampsa Pursiainen^a

^a*Computing Sciences, Tampere University (TAU), PO Box 692, 33101, Tampere, Finland*

^b*Aix-Marseille Univ., CNRS, Centrale Marseille, Institut Fresnel, Marseille, France*

Abstract

This paper aims to reconstruct the internal structure of a two-dimensional test object via numerically simulated full-wave time domain radar tomography with the presence of carrier wave induced (carrier-induced) uncertainty, following from a complex domain structure, and short wavelength of the signal as compared to the target object diameter. In particular, we consider an application in planetary scientific studies of reconstructing the interior structure of an arbitrary high contrast small Solar System Body (SSSB), i.e., an asteroid, with a probing signal of small wavelength following from the instrument and mission payload limitations. Our uncertainty reduction model is devised from the statistical viewpoint by finding the reconstruction via multiple datasets assuming that the carrier-induced deviations in the reconstruction correspond to random deviations, which are independent and identically distributed (IID) for each dataset. A spatial and frequency-based error marginalisation is implemented, thus inspecting the relationship between the signal baseband frequency and the phase discrepancy of the modelling accuracy, determined by the signal and domain parameters. The numerical experiments are performed for 20 and 60 MHz center frequencies proposed for CubeSat-based radars. Of these, the latter matches the center frequency of the Juventas Radar which will be aboard HERA mission to investigate the interior structure of asteroid Dimorphos, the asteroid moon of the binary system 65803 Didymos.

Keywords: Asteroids, compositions, interiors, radar observations, image processing

1. Introduction

Radar tomography (RT) has emerged as a powerful technique for obtaining high resolution images of complex target domains in recent years. With the application of tomographic radar imaging spanning across several fields of research, such as biomedical imaging, geoscience, and engineering; sophisticated and computationally efficient inversion techniques to characterise the interior properties of such a target domain, from the scattered field of the probing radar signal

Email address: yusuf.yusuf@tuni.fi (Yusuf Oluwatoki Yusuf)

have also been developed extensively [1, 2, 3, 4, 5, 6]. The inverse scattering problem of full-wave tomography, however, has some bottlenecks that can increase modelling uncertainties, resulting in a less accurate reconstruction of the target domain. This paper aims at reconstructing the interior structure of a complex domain, e.g., an arbitrary high contrast Small Solar System Body (SSSB), via full-wave time domain RT, and specifically, investigating the phase and wavelength-induced errors; which follow as a consequence of complex multipath signal propagation inside the target due to high contrast details in the permittivity distribution.

The first attempt to use RT to recover the interior structure of an SSSB was the COMET Nucleus Sounding Experiment by Radio-wave Transmission (CONSERT) [7, 8], which was part of the European Space Agency’s (ESA) Rosetta mission to comet 67P/Churyumov-Gerasimenko. The emergence of small spacecraft technology as a part of deep space missions has improved the future possibilities to perform RT investigations of SSSBs with a sufficient signal coverage [9, 10]. Such a plan is included in ESA’s coming Hera mission; the Juventas CubeSat carried by the Hera probe will perform tomographic radar measurements of Dimorphos, the asteroid moon of 65803 Didymos, with its Juventas Radar (JuRa) [11, 12]. In JuRa, the centre frequency is 60 MHz, i.e., the wavelength is 5 m outside and approximately 2.5 m inside the target, the bandwidth is 20 MHz, while the diameter of Dimorphos is about 160 m, i.e., approximately 64 times the wavelength propagating inside.

In this study, we concentrate on full-wave modelling, a necessary tool to distinguish the scattering originating from different parts of the domain, for example, surface and interior structures [13]. This requires that the differences between the modelled and measured field are small enough compared to the measurement inaccuracies. Our focus is suppressing the effects of these inaccuracies in the reconstruction process which is of utmost importance, e.g., based on the recent numerical study [14].

In full-wave modelling with the finite element time domain (FETD) method [5, 15], the carrier-induced effects in the modulated signal can result in modelling or measurement errors produced by (1) phase and wavelength-induced factors, (2) domain discretization, (3) wave propagation accuracy, and (4) numerical inaccuracy due to noise in demodulation of the carrier signal. This study concentrates on the errors due to (1), phase inaccuracy and wavelength-induced effects, which are due to the short wavelength of the signal as compared to the target object diameter, and propagation through a high contrast domain. To marginalise these errors, we propose a Gaussian prior model for the uncertainty of the phase in form of a discrepancy function. This discrepancy gives the maximum limit for the applicable baseband frequency considering the real part of the permittivity that can be reconstructed. The experiments show how the discrepancy-based prior model, combined with total variation regularised inverse approach, allows for the marginalisation of the carrier-induced effects via independence sampling. The results also show how data obtained for a dense spatial point distribution can be effectively utilised in the process of marginalising carrier-induced effects, taking into account the Nyquist sampling condition for both the modulated and demodulated wave.

This article is organised into Section 2 through Section 4. Section 2 focus on the model description, and statistical formulation of spatial and frequency-based error marginalisation process. Furthermore, the total variation inversion technique and the truncated singular value decomposition filtering are discussed in Section 2.4. In Section 2.5, the experimental setup and signal

configurations are highlighted, and the corresponding parameters related to the numerical implementation are documented appropriately. Section 3 includes the numerical results for the two dimensional analogue model and the discussions of these results are presented in Section 4.

2. Materials and methods

2.1. Inverse wave propagation problem

We consider transverse electric (TE) wave propagation in which the total electric field u propagating in the horizontal plane is oriented along the vertical direction. The TE-field satisfies the wave equation

$$\epsilon'_r \frac{\partial^2 u}{\partial t^2} + \sigma \frac{\partial u}{\partial t} - \Delta u = \frac{\partial \mathfrak{B}}{\partial t} \quad (1)$$

in a given spatio-temporal domain $[0, T] \times \Omega$, in which the spatial part includes the scattering target Ω_1 and its near surroundings Ω_2 . Here, ϵ'_r is the real part of the relative permittivity $\epsilon'_r = \epsilon_r - j\epsilon''_r$, σ is the conductivity $\sigma = 2\pi f\epsilon''_r$, f denotes the signal frequency, and $\partial \mathfrak{B}/\partial t$ is a point source term for which $\mathfrak{B} = \mathfrak{B}(t, \vec{p}_0)$ is the current density of a vertical antenna set at point \vec{p}_0 . The spatial scaling is assumed to be such that the velocity of the wave in vacuum is one ($c = 1$). The time t , position \vec{x} , permittivity ϵ'_r , conductivity σ , and velocity $c = \epsilon'^{-1/2}_r$ can all be scaled to SI-units through the expressions $s c_0^{-1} t$, $s \vec{x}$, $\epsilon_0 \epsilon'_r$, $s^{-1} \epsilon_0 c_0^{-1} \sigma$, and $c_0 c$, respectively. Here, s is a spatial scaling factor (meters), $c_0 = (\epsilon_0 \mu_0)^{-1/2}$ is the speed of the electromagnetic wave in vacuum, $\epsilon_0 = 8.85 \cdot 10^{-12}$ F/m is the electric permittivity of vacuum, and $\mu_0 = 4\pi \cdot 10^{-7}$ H/m is the magnetic permeability which is assumed to be constant in Ω .

The domain is assumed to be decomposed by a triangular mesh $\mathcal{T} = \{T_1, T_2, \dots, T_M\}$, whose j -th triangle \mathcal{T}_j corresponds to a set indicator function χ_j , with $\chi_j(\vec{x}) = 1$ if $\vec{x} \in T_j$ and $\chi_j(\vec{x}) = 0$ otherwise. The mesh \mathcal{T} discretises the real relative permittivity as given by $\epsilon'_r = \tilde{\epsilon}'_r + \sum_{j=1}^M s_j \chi_j$, where $\tilde{\epsilon}'_r$ is a constant background permittivity and s_j is the corresponding coefficient of χ_j . Replacing the total electric field u in the wave equation (1) by its partial derivative with respect to s_j results in

$$\epsilon'_r \frac{\partial^2}{\partial t^2} \left(\frac{\partial u}{\partial s_j} \right) + \sigma \frac{\partial}{\partial t} \left(\frac{\partial u}{\partial s_j} \right) - \Delta \frac{\partial u}{\partial s_j} = - \frac{\partial}{\partial t} \left(\frac{\partial h}{\partial s_j} \right), \quad (2)$$

where h on the right-hand side is referred to as the scattering source which follows from Ampere's law, and relates directly to \mathfrak{B} , as $\mathfrak{B} = \frac{\partial h}{\partial s_j}$. Here, h is denoted by

$$h = \epsilon'_r \frac{\partial u}{\partial t} = \sum_{j=1}^M s_j \chi_j \frac{\partial u}{\partial t} - \tilde{h} \quad \text{with} \quad \tilde{h} = \tilde{\epsilon}'_r \frac{\partial u}{\partial t}, \quad (3)$$

hence, its partial derivative with respect to s_j gives $\partial h / \partial s_j = \chi_j \partial u / \partial t$. The scattering source can be interpreted as the source of the differentiated wave and is estimated via the Born approximation, i.e., by replacing the total field u with the incident field as described in Van Hove [16], Chew and Wang [1], Sorsa et al. [17].

The wavefield is assumed to consist of two complex quadrature amplitude modulated (QAM) components [18]. The components of QAM consist of the in-phase and quadrature component, of

which, the latter has a $\pi/2$ phase difference compared to the in-phase signal. Consequently, the amplitude of the signal can be obtained accurately anywhere in the spatio-temporal domain. The reconstruction process utilises baseband frequency data \mathbf{y} obtained via QAM demodulation as a full wave recorded for time steps t_1, t_2, \dots, t_N at spatial points $\vec{p}_1, \vec{p}_2, \dots, \vec{p}_K$. The data corresponds to the difference between the wavefields $u(t, \vec{p}_i)$ and $\tilde{u}(t, \vec{p}_i)$ associated with the actual real relative permittivity distribution ϵ'_r and its background estimate $\tilde{\epsilon}'_r$. Using the differentiated signal, this difference can be estimated as follows:

$$y_j(t) = \mathfrak{D}\mathfrak{M}[u(t, \vec{p}_i) - \tilde{u}(t, \vec{p}_i)] = \mathfrak{D}\mathfrak{M} \left[\sum_{j=1}^M s_j \frac{\partial}{\partial s_j} u(t, \vec{p}_i) \right], \quad (4)$$

where $\mathfrak{D}\mathfrak{M}$ denotes a QAM demodulation operator. Defining Jacobian matrices \mathbf{J}_ℓ with

$$(\mathbf{J}_\ell)_{i,j} = \mathfrak{D}\mathfrak{M} \left[\frac{\partial}{\partial s_j} u(t_\ell, \vec{p}_i) \right], \quad (5)$$

one obtains a linearized forward model

$$\mathbf{y}_\ell = \mathbf{J}_\ell \mathbf{x} + \mathbf{n}_\ell \quad \ell = 1, 2, \dots, N, \quad \text{i.e.,} \quad \mathbf{y} = \mathbf{L} \mathbf{x} + \mathbf{n} \quad (6)$$

for the inverse problem of reconstructing \mathbf{x} given the data \mathbf{y} . Here,

$$\mathbf{y} = \begin{pmatrix} \mathbf{y}_1 \\ \mathbf{y}_2 \\ \vdots \\ \mathbf{y}_N \end{pmatrix}, \quad \mathbf{L} = \begin{pmatrix} \mathbf{J}_1 \\ \mathbf{J}_2 \\ \vdots \\ \mathbf{J}_N \end{pmatrix}, \quad \text{and} \quad \mathbf{n} = \begin{pmatrix} \mathbf{n}_1 \\ \mathbf{n}_2 \\ \vdots \\ \mathbf{n}_N \end{pmatrix}. \quad (7)$$

The matrix \mathbf{L} determines the linearized effect of the scatterers on the data \mathbf{y} as a function of the perturbation of the exact discretized real relative permittivity \mathbf{x} and the vector \mathbf{n} is the noise term.

2.2. Wave propagation in high and low contrast medium

We focus on inverting equation (6) under the assumption that \mathbf{L} contains inevitable modelling errors following from phase inaccuracies in the wave simulations. The carrier wave, in which the inputs are imposed, has a much higher frequency than the baseband signal. In QAM, the transmitter uses the input signal to vary the carrier's amplitude, hence creating a modulated signal. Signals modulated with a high frequency lead to a phase error at the demodulation stage, depending on the electromagnetic properties of the target domain.

Specifically, a wavefield propagated through a complex domain undergoes changes as a result of permittivity variations within the spatial domain leading to effects such as refraction and reflection, on the material boundaries. The boundary effects give rise to changes in the wave amplitude, phase, and direction of propagation depending on the contrast of the medium described by the refractive index [20]. The greater the refractive index is, the stronger the effects are. The refractive index $n = c_0/c = \sqrt{\epsilon'_r}$ is obtained as the ratio of the free space velocity c_0 and the velocity c in the medium, or alternatively, via the real relative permittivity ϵ'_r when the permeability of the

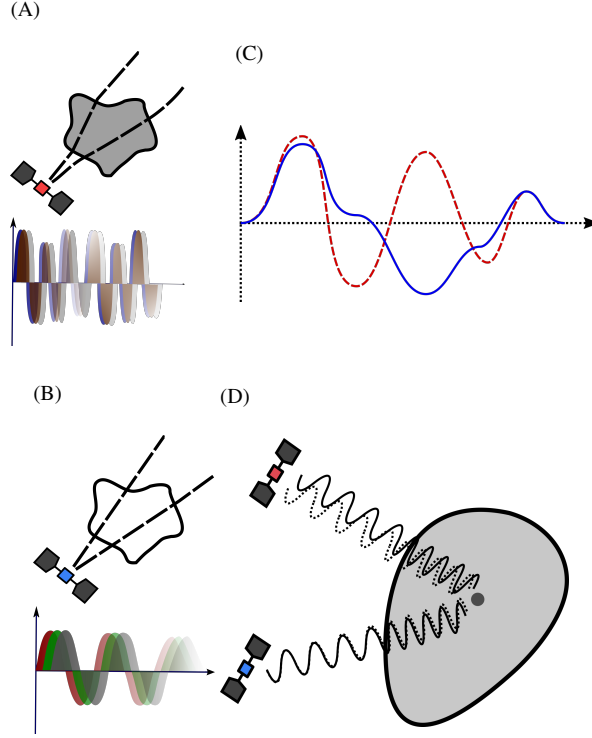


Figure 1: Forward modelling error sources, their effect and discrepancy. Schematic illustration of signal propagation in high contrast (A) and low contrast (B) domain and the corresponding signals, depicting phase errors in each case. Since the velocity of the wave, and thereby wavelength, decreases when the contrast increases, the phase errors in the forward model are likely to increase along with the contrast [19]. Moreover, the increase in the probing signal energy concentrated at the target surface is likely to increase the amplitude errors, resulting into larger refraction in the high contrast medium due to increased deviations from the signal energy. (C) Modelling errors in the carrier phase can lead to large random fluctuations in the demodulated baseband data; three of the local maxima of the demodulated red dashed wave coincide with those of the blue wave, but with flipped signs due to opposite phase of the carrier. (D) Two signals (solid and dotted wave) can be considered to be in the same phase if the phase angle difference is less than or equal to a quarter of pi, i.e., $\phi \leq \pi/4$. We assume that this discrepancy condition is satisfied for a wavefield propagating the length ℓ inside the target Ω with real relative permittivity ϵ'_r , if the maximum frequency of the wavefield is less than or equal to the baseband frequency (pulse bandwidth) f_B , and if the uncertainty of these parameters satisfies the discrepancy condition in equation (16).

material is that of a vacuum. Since the frequency is maintained everywhere in the medium, there is a smaller velocity and a shorter wavelength in the high-contrast (high permittivity) target than in free space or low-contrast target. Hence, the complexity of the wave propagation, and thereby the likelihood of phase modelling errors increases along with the value of the refractive index; See Figure 1.

2.3. Prior model for carrier-induced uncertainty

Carrier-induced uncertainty in a propagated wave signal can be viewed from the spatial and spectral perspectives. The Nyquist sampling criterion plays an important role in determining the number of points, sampled from a non-zero wave signal. We consider a pulse of length T and pulse bandwidth $1/T = f_B \leq B$ which matches the twice maximal frequency of the demodulated

signal and is bounded by the radar bandwidth B from above; See Figure 2.

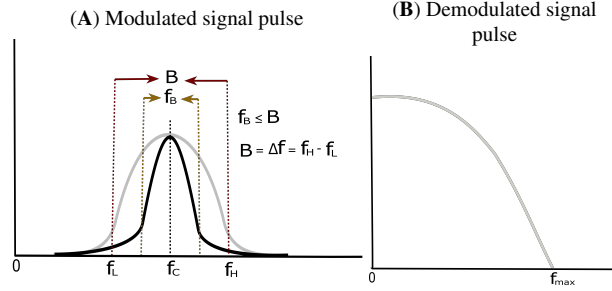


Figure 2: Schematic diagram of (A) modulated and (B) demodulated signal pulses. The radar bandwidth B bounds the pulse bandwidth f_B from above, implying the propagated pulse is always limited by the instrument capacity. Here, f_H and f_L are the upper and lower cut-off frequencies respectively, f_c is the centre frequency of the modulated signal pulse, while f_{\max} is the maximum frequency of the demodulated signal pulse.

The pulse is modulated via the QAM approach which incorporates an in-phase and quadrature components into the signal resulting in the centre frequency f_{centre} , corresponding to the centre of the spectrum with a pulse bandwidth f_B . The Nyquist criterion is defined by the spatial and temporal sampling rate S_s and S_t , stating $S_s \geq 2f_{\max}c$ and $S_t \geq 2f_{\max}$. This implies that, the QAM demodulated baseband signal can be captured fully, if the sampling frequency is greater than double the highest frequency f_{\max} contained in the baseband signal [21]. In case of QAM, $f_{\max} = f_B/2$ i.e., the maximum pulse frequency corresponds to half the pulse bandwidth for a smooth pulse. We use the first derivative Blackman-Harris (BH) pulse, which is employed often in geophysical FETD modelling applications as the probing pulse of a radar signal. The modulated signal is transmitted and propagated through the tomographic target Ω_1 , after which it is demodulated to obtain the final simulated measurement data \mathbf{y} containing frequencies on the baseband frequency interval $[0, f_{\max}]$.

2.3.1. Model for grid reduction

The principles of compressed sensing, see, e.g., [22], provide a viable means to reduce the carrier-induced uncertainties. That is, a sparse and a stable reconstruction of the unknown permittivity can be obtained utilising a reduced data coverage in the reconstruction process. To avoid phase errors in the eventual signal, i.e., the demodulated data wave, a statistically motivated approach is needed to reduce spatial uncertainty. We assume that the pulse bandwidth is optimal with respect to the modelling accuracy. In the sense that any data fluctuations \mathbf{z} related to frequencies higher than that of the demodulated wave, i.e., the pulse bandwidth f_B , are noisy due to modelling inaccuracies, and therefore, constitute a nuisance to be marginalised out of the final estimate. Associating the unknown permittivity distribution \mathbf{x} with a conditional posterior probability density of \mathbf{x} given \mathbf{y} and \mathbf{z} , $\pi(\mathbf{x} | \mathbf{y}, \mathbf{z})$, the effect of \mathbf{z} on \mathbf{x} in which both are dependent, can be marginalised as [23]:

$$\pi(\mathbf{x} | \mathbf{y}) = \int_{\mathbb{R}^m} \pi(\mathbf{z}) \pi(\mathbf{x} | \mathbf{y}, \mathbf{z}) d\mathbf{z}, \quad (8)$$

where $\pi(\mathbf{z})$ is a density for the modelling errors, especially phase errors; $\pi(\mathbf{x} | \mathbf{y})$ is the marginalised density, and \mathbb{R}^m is the space of \mathbf{z} . Furthermore, the expectation of \mathbf{x} given the data \mathbf{y} can be ob-

tained as:

$$\mathbb{E}(\mathbf{x} | \mathbf{y}) = \mathbf{x}^\dagger = \int_{\mathbb{R}^n} \mathbf{x} \pi(\mathbf{x} | \mathbf{y}) d\mathbf{x}, \quad (9)$$

where \mathbb{R}^n is the space of \mathbf{x} . In our current approach, \mathbf{x} given \mathbf{y} and \mathbf{z} is determined by a classical regularised inversion scheme, that is, the conditional distribution of \mathbf{x} given \mathbf{y} and \mathbf{z} corresponds to Dirac's delta function. Substituting equation (8) in equation (9) where $\pi(\mathbf{x} | \mathbf{y}, \mathbf{z})$ is replaced with the Dirac delta function $\delta(F(\mathbf{y}, \mathbf{z}) - \mathbf{x})$. According to the Dirac delta function sifting property, this gives

$$\mathbf{x}^\dagger = \int_{\mathbb{R}^m} \int_{\mathbb{R}^n} \mathbf{x} \delta(F(\mathbf{y}, \mathbf{z}) - \mathbf{x}) d\mathbf{x} \pi(\mathbf{z}) d\mathbf{z}. \quad (10)$$

The simplest model is to assume that the wavelength-induced phase errors are IID and that the posterior is set by a deterministic function $\mathbf{x} = F(\mathbf{y}, \mathbf{z})$. Thus the expectation is obtained as

$$\mathbf{x}^\dagger = \int_{\mathbb{R}^m} F(\mathbf{y}, \mathbf{z}) \pi(\mathbf{z}) d\mathbf{z}. \quad (11)$$

Equation (11) can be resolved by Monte Carlo computation to save computational resources [24]. However, to ensure convergence of the sampling, the realisations \mathbf{z}_k should be sampled from the distribution $\pi(\mathbf{z})$ or an arbitrary distribution $\mathbf{g}(\cdot)$ very close to $\pi(\mathbf{z})$, and assumed to be uniform in this case. The law of large numbers and central limit theorem motivates the convergence, and the convergence rate $\mathcal{O}(N^{-1/2})$ of the sample based mean

$$\frac{1}{K} \sum_{k=1}^K F(\mathbf{y}, \mathbf{z}_k) \rightarrow \mathbf{x}^\dagger, \quad \text{when } K \rightarrow \infty. \quad (12)$$

To formulate this approach for spatial point sets, we define sets \mathcal{P}_k and \mathcal{Q} in which the mutual distance between any two points is less than or equal to $\lambda_{f_{\max}}/2 = c_0/(2f_{\max})$ and $\lambda_{\text{centre}}/2 = c_0/(2f_{\text{centre}})$, respectively. That is, \mathcal{P}_k is dense enough to satisfy the spatio-temporal Nyquist criterion w.r.t. the information content of the scattered field [25]. It is further assumed that \mathcal{Q} contains the full set of measurement points and \mathcal{P}_k , $k = 0, 1, 2, \dots, K$ with an equal number of points in each is its subset, $\mathcal{P}_k \subset \mathcal{Q}$. As the measurements are inverted after the QAM demodulation, if modelling errors are absent, each dataset to be inverted has a full coverage when the criterion w.r.t. f_{\max} is satisfied. However, due to the existence of the modelling errors, each dataset satisfying this criterion needs to be considered rather as a subset of the full data fulfilling the criterion w.r.t. f_{centre} . As we consider the modelling error for a given set to be a random variable, the sample based mean in equation (12) can be realised by first finding a suitable point set sample \mathcal{P}_k which can be obtained either by a regular or randomised point selection process.

2.3.2. Model for phase error formation

A complementary approach to reduce uncertainty in the spectral sense is to apply a discrepancy condition. Assuming that the phase angle shift between the modelled and measured demodulated signal is maximally $\pi/4$. We assume that the signal is measured for a two-way path whose length inside the target is ℓ . If the signal penetrates to the centre of the target from each direction, providing a full signal coverage for the interior, then ℓ can be associated with the largest diameter

of the target. In order to maintain the phase angle difference within the interval $[0, \pi/4]$, the path length per wavelength inside the target, defined as

$$N = \ell / \lambda_f = \frac{\sqrt{\epsilon'_r} f \ell}{c_0}, \quad (13)$$

for the modelled and measured wavefield, must not differ more than $\pi/4$ in phase which is equivalent to one-eighth of the pulse cycle. This gives rise for the following definition of the phase discrepancy, d , which is based on the maximum relative difference of N :

$$d = \frac{N + \frac{1}{8}}{N} - 1 = \frac{8 \sqrt{\epsilon'_r} f \ell + c_0}{8 \sqrt{\epsilon'_r} f \ell} - 1, \quad (14)$$

where ϵ'_r represents the average real relative permittivity of the target. The maximum deviation between N_{sim} and N resulting from the simulated and actual wave propagation is, thereby,

$$1 - d \leq \frac{N_{sim}}{N} \leq 1 + d \quad \text{or} \quad \left| \frac{\Delta N}{N} \right| \leq d, \quad (15)$$

where $\Delta N = N_{sim} - N$. By combining the equations (13) and (15), this can be expressed in terms of absolute total derivative as

$$\frac{|\Delta \epsilon'_r|}{2 \sqrt{\epsilon'_r}} + \frac{|\Delta f|}{f} + \frac{|\Delta \ell|}{\ell} \leq d. \quad (16)$$

Firstly, this inequality allows for estimating the discrepancy, given the uncertainty of the *a priori* real relative permittivity estimate ϵ'_r and that of the path length ℓ , i.e., the more complex the geometry and the higher the contrast of the domain the more uncertain ℓ . Secondly, together with the definition of the discrepancy in equation (14), it also enables estimating the maximal bandwidth applicable in the measurement; that is, the discrepancy implied by the permittivity, path length and frequency deviation should coincide with the *a priori* uncertainty estimates obtained for these quantities. Thirdly, the uncertainty implied by equation (16) can be incorporated into the forward modelling process through a surrogate approach, assuming that all uncertainty follows from frequency deviation Δf , which refers to the possible frequency fluctuations of the modulated signal which are reflected to the baseband data through the demodulation process. Since the effect of such deviations can be evaluated via signal demodulation, one can use surrogate approach which allows avoiding repetitive and computationally expensive wave simulations. We define a surrogate frequency f_s to be a Gaussian random variable with mean f_m and standard deviation d matching with the discrepancy, i.e.,

$$f_s = f_m + d\mathbf{r}, \quad (17)$$

where \mathbf{r} is a zero-mean Gaussian random variable with standard deviation equal to one and f_m is the actual centre frequency f_{centre} . The formulation in equation (17) models the uncertainty in the surrogate frequency f_s , considering uncertainty in the frequency as described in equation (16). This is further described in section 2.5.2 and implemented in the case of randomised averaging approach experiments in this study.

2.4. Inversion techniques

Full-wave tomography is challenging, partly because there is a need to select an inversion method, that appropriately solves the problem of reconstructing scattered waves from the target domain. Expectedly, there is a trade-off between the performance and complexity of several inversion methods available.

2.4.1. Total variation

Total variation (TV) is an inversion method that has evolved from image denoising application to more robust applications of inverse problems [26]. It has been found to be stable in tomographic reconstruction of distributional information based on sparse data and to even enable finding a perfect reconstruction assuming that the distribution to be reconstructed is also sufficiently sparse [17, 27, 28]. We obtain a TV regularised solution \mathbf{x} of the linearized forward model following the approach of [5, 15], i.e.,

$$\mathbf{x}^\dagger = \mathbf{L}^* \mathbf{y}, \quad (18)$$

$$\mathbf{x}_{l+1} = (\mathbf{L}^* \mathbf{L} + \alpha \mathbf{D}^T \Gamma_l \mathbf{D})^{-1} \mathbf{x}^\dagger. \quad (19)$$

Here, \mathbf{x}^\dagger is a backpropagated estimate for \mathbf{x} , Γ_l is the weighting matrix limiting the magnitude of x , to avoid numerical instability due to division by a very small value; D is a positive definite and invertible derivative operator defined as

$$D_{i,j} = \beta I_{i,j} + \frac{(2I_{i,j} - 1) \int ds}{\max_{i,j} \int ds},$$

where $I_{i,j} = 1$ if $i = j$, $I_{i,j} = 0$ if $i \neq j$, and α and β are the regularisation and smoothing parameters of the solution. The final reconstruction is found as a vector containing the absolute value of the entries in the final iterate.

2.4.2. Filtering via truncated singular value decomposition

Singular value decomposition (SVD) [29] is a traditional means of data compression. We combine the statistical approach described in Section 2.3 with the truncated SVD (TSVD) to filter spatio-temporal data [30]. This is motivated by the assumption that scattering consists of separate scattering patterns $n = 1, 2, 3, \dots, m$, organised in descending order by their amplitude. The spatial pattern and time-dependence are described by two orthogonal sets of vectors $\mathbf{u}_1, \mathbf{u}_2, \dots, \mathbf{u}_m$ and $\mathbf{v}_1, \mathbf{v}_2, \dots, \mathbf{v}_m$. The vector entries in \mathbf{u}_n and \mathbf{v}_n correspond to the spatial points and time steps of the measurement, respectively. Consequently, the matrix $\mathbf{Y} = (\mathbf{y}_1, \mathbf{y}_2, \dots, \mathbf{y}_N)$ contains the full data and the TSVD filter is defined as follows:

$$\mathbf{x}^\dagger = \mathbf{L}^* \mathbf{y} \approx \sum_{n=1}^p \sigma_n \mathbf{K}_n^* \mathbf{u}_n, \quad \text{where} \quad \mathbf{K}_n = \sum_{\ell=1}^N \bar{v}_{\ell,n} \mathbf{J}_\ell, \quad (20)$$

σ_ℓ denotes the amplitude of the n -th most intense pattern, and $p \leq m$ is selected so that the energy corresponding to the remaining sum is approximately that of the noisy signal, i.e., $\sum_{n=p+1}^m \sigma_n^2 =$

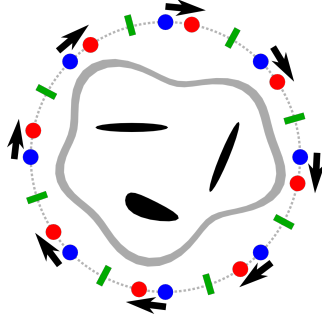


Figure 3: The target Ω_1 applied in the two-dimensional numerical simulations. It consists of an interior part, three voids and a surface layer (mantle), these are given the complex relative permittivity values $\epsilon_r = 4.0 + j0.03$, $\epsilon_r = 1.0$, and $\epsilon_r = 3.0 + j0.02$, respectively. The real part ϵ'_r of the relative permittivity distribution is visualised on a decibel scale with respect to $\epsilon'_r = 4.0$ as a background value. The orbit used in the numerical experiments is visualised by the circle surrounding the target. The blue and red dots depict two monostatic signal configurations with uniform distance between the points on the synthetic orbit, i.e., a circle surrounding the target. In the regular averaging approach, such monostatic point sets are obtained by rotating an initial set as shown by the arrows and, thus, covering each point in the full set of measurements. In the randomised averaging approach, a uniformly distributed random point is picked independently from each sector, whose length satisfies the Nyquist criterion w.r.t. the demodulated signal pulse as described in Section 2.3.1. The sectors are depicted by the intervals between the green lines. The complete measurement point set including all the sectors satisfies the Nyquist criterion w.r.t. the centre frequency of the signal.

$\|\mathbf{n}\|_2^2$. In essence, we choose p such that $\sum_{i=1}^p \sigma_i^2 / \sum_{n=1}^m \sigma_n^2 \geq 1/(1 + 10^{-\frac{\mu}{20}})^2$, where $i = 1, \dots, m$ and μ is the noise level. The right hand side provides a lower bound by the assumption that the amplitude of the noisy signal is a sum of the noiseless and noisy signals.

In this study, the TSVD approach is applied in the backpropagation part in equation (18) of the TV regularisation process. We compare its performance to the case of full data. Here, $\mathbf{K}_n^* \mathbf{u}_n$ can be interpreted as a backpropagated pattern \mathbf{u}_n with intensity σ_n and time dependence \mathbf{v}_n . This formulation of TSVD is used, since the scattering patterns are assumed to be well localised in the time domain.

2.5. Numerical Experiments

2.5.1. Two-dimensional domain

In the numerical experiments, we investigate inverting full-waveform data in two dimensions using the target Ω_1 of [17] with unitless diameter 0.28 scaled to the estimated diameter 160 m ($s = 571$) of Dimorphos; see Figure 3. The interior part of Ω_1 is given the relative real permittivity $\epsilon'_r = 4$ excluding three voids with vacuum permittivity ($\epsilon'_r = 1$) and a surface layer (mantle) with real relative permittivity value of $\epsilon'_r = 3$. The permittivity of asteroid minerals such as kaolinite and dunite match roughly these values regarding solid and powder composition for the interior and surface layer, respectively. The loss tangent δ which determines the imaginary part of the complex relative permittivity $\epsilon_r = (1 + i\delta)\epsilon'_r$ is considered as a nuisance parameter. We set δ to be in the range from 0.0005 to 0.04 proposed for asteroid minerals in [31].

2.5.2. Signal specifications

We apply QAM modulated Blackman-Harris window as a signal pulse centred at (A) 20 and (B) 60 MHz frequencies covering the bandwidths of 10 and 20 MHz, respectively; See Table 1 and

Figure 4. The centre frequency of 20 MHz has been proposed as a potentially feasible low end for a CubeSat-based penetrating radar exploration in a recent concept study [9], while 60 MHz will be applied in the JuRa investigation [32, 11]. The general knowledge of asteroid composition and radar signal penetration suggests that the centre frequency should be between 10 and 100 MHz [33, 31] in order to enable full coverage of the wavefield inside the target.

Table 1: Blackman-Harris signal pulses and their corresponding frequencies, bandwidths, and durations.

Signal pulse	Centre freq. (MHz)	Bandw. (MHz)	Duration (μ s)	Cycles per pulse
(A)	20	10	0.190	4
(B)	60	20	0.095	5.5

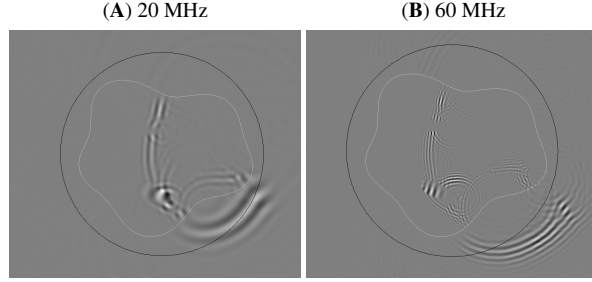


Figure 4: Signal propagation path in the two-dimensional domain for the signal pulse (A) 20 and (B) 60 MHz. The 20 MHz signal has a single strong wavefront propagating through the domain with the intensity implying how much of the domain details can be reconstructed. The 60 MHz signal has multiple weak wavefronts propagating through the domain, a potential source of phase and wavelength-induced uncertainty.

We consider the following four monostatic signal configurations (I)–(IV) (Figure 3, Table 2) for obtaining the full-wave data. These differ by the averaging and filtering strategy applied to process the data. The averaging process utilises the simulated full-wavefield which has been obtained around the tomographic target with spatial and temporal resolution satisfying the Nyquist criterion with respect to the centre frequency.

The regular averaging approach is a systematic selection of measurement points at uniform angular distances from each other. The points are independently selected at intervals corresponding to the spatial sampling rate S_s . Since the systems for the signal pulses (A) and (B) have a total of 128 and 384 points, respectively. In total 32 (sparse) and 64 (dense) points are sampled from the signal pulse system (A), while 64 (sparse) and 128 (dense) points are sampled from the signal pulse (B) system. To ensure that the resulting point sets cover the full set of measurement data, multiple selections of averaged points are sampled. In essence, the regular averaging approach essentially has 4×32 (sparse) and 2×64 (dense) points for the signal pulse (A) system, and 6×64 (sparse) and 3×128 (dense) points for the signal pulse (B) system. The multiple terms in the regular averaging approach are referred to as the regular turns in Table 2, and illustrated in Figure 3. Two different spatial resolutions, sparse and dense, are considered for the single point averaged

Table 2: Spatial resolution of the full dataset before and after the averaging process with their corresponding averaging techniques. The approach to the spatial averaging in configurations (I)–(IV) of the numerical experiments is described in Figure 3, and the signal pulses (A) 20 and (B) 60 MHz described in Table 1. The 3rd and 4th columns give the total and averaged number of spatial points in the full dataset and after the averaging process, respectively. The 5th column includes the number of turns in the regular averaging process for each averaging resolution, and the 6th gives the number of spatial point sets and frequencies applied in the randomised averaging. The last column indicates the type of filtering applied to each case in the experiment.

Signal pulse	Signal configuration	Total points	Spatial averaging	Regular turns	Randomised turns/frequency	Filter
(A)	(I)	128	dense/ 64	2	-	None
	(II)	128	dense/ 64	2	-	TSVD
	(III)	128	dense/ 64	-	8/5	None
	(IV)	128	dense/ 64	-	8/5	TSVD
	(I)	128	sparse/ 32	4	-	None
	(II)	128	sparse/ 32	4	-	TSVD
	(III)	128	sparse/ 32	-	8/5	None
	(IV)	128	sparse/ 32	-	8/5	TSVD
(B)	(I)	384	dense/ 128	3	-	None
	(II)	384	dense/ 128	3	-	TSVD
	(III)	384	dense/ 128	-	8/5	None
	(IV)	384	dense/ 128	-	8/5	TSVD
	(I)	384	sparse/ 64	6	-	None
	(II)	384	sparse/ 64	6	-	TSVD
	(III)	384	sparse/ 64	-	8/5	None
	(IV)	384	sparse/ 64	-	8/5	TSVD

signal in this study. The sparse cases have an average point density corresponding to the Nyquist criterion for the pulse bandwidth, and the dense cases have twice as much of the point density of the sparse cases.

Furthermore, in the randomised averaging, the centre frequency is slightly perturbed by varying the estimated centre frequency in the demodulation process according to the discrepancy condition in equation (17). In essence, we run the simulation for 5 different centre frequency realisations, using the discrepancy d as the standard deviation and actual centre frequency f_{centre} as the mean f_m . Hence, each set of single averaged point is averaged over 5 different frequencies and then all 8 sets spatially. The sampling rate of the regular averaging approach was retained, hence, giving a system with similar single averaged points, i.e., 32 (sparse) and 64 (dense) points from the signal pulse (A) system, and 64 (sparse) and 128 (dense) points from the signal pulse (B) system. However, the multiple selection of the single averaged points was fixed to 8 for both sparse and dense points of the two systems. This guarantees that every point has the chance to be selected

and the full coverage of the data is ensured since a uniformly distributed random point is selected from each sector illustrated by the green lines in Figure 3.

In configurations (I) and (II), regular spatial averaging is applied to nonfiltered (full) data in (I) and TSVD filtering (II). Configurations (III) and (IV) utilise a randomised point set and frequency perturbed data with full data (III) and TSVD filtering (IV).

2.5.3. Noise

The measurement noise was simulated by adding Gaussian white noise to the modulated signal. The inversion results are obtained for two different magnitudes of the noise. With the lower noise level, the signal-to-noise ratio (SNR) of the simulated data was 20 dB, and with the higher one it was 12 dB. The higher SNR is motivated by the observations of the CONSERT team suggesting that the main signal peak of the measurement was found to have at least 20 dB SNR with respect to noise peaks [8]. The lower SNR has been set based on recent numerical and experimental modelling studies [34, 13, 18] suggesting that an SNR above 10 dB might be sufficient for reconstructing the internal permittivity of a complex-structured asteroid analogue and that such an accuracy between a numerically modelled field and a laboratory measurement can be achieved experimentally. The experimental setup in Table 2 was implemented for both noise 20 and 12 dB noise cases.

2.5.4. Similarity and Error Measures

To analyse the accuracy of the reconstructions in different parts of the target Ω_1 , we define sub-domains \mathcal{S}_1 (voids) and \mathcal{S}_2 (surface layer) restricted by the contours of the permittivity distribution in a descending order. The structural similarity (SSIM) of the reconstruction to the exact distribution is computed to measure the quality of the reconstructed image relative to the background [35]. We also evaluate the Mean Squared Error (MSE) between the exact distribution and reconstruction for Ω_1 , \mathcal{S}_1 and \mathcal{S}_2 . The Overlap Error (OE) between the detail \mathcal{S}_i and a reconstructed permittivity perturbation is defined as the ratio

$$\text{area}(\mathcal{S}_i \cup \mathcal{O}_i) / \text{area}(\mathcal{S}_i), \quad (21)$$

where $\mathcal{O}_i = \bigcup_{i \in I_\zeta} T_i$ is a set composed by triangles T_i in the index set I_ζ which includes the most intense part of the reconstructed distribution with surface area equals to that of the given detail excluding the sets \mathcal{O}_j for $j = 1, 2, \dots, i-1$, that is, $I_v = \{i \mid |x_i| \geq v, T_i \in \Omega_1 \setminus \bigcup_{j=1}^{i-1} \mathcal{O}_j\}$ and $\zeta = \arg \max_v \{\sum_{i \in I_v} \text{area}(T_i) \leq \text{area}(\mathcal{S}_i)\}$.

The Wilcoxon rank sum (WRS) test, a nonparametric alternative to the two-sample t-test for two populations X and Y of assumably independent samples, was used to analyse the significance of the differences observed. The WRS tests the null hypothesis that data in X and Y are samples from continuous distributions of equal medians, against the alternative that they are not, with the assumption that the samples are independent [36].

2.5.5. Numerical implementation

The computations are implemented using the openly available GPU-Torre package¹ [17], which utilises the Matlab platform (Mathworks, Inc.). GPU-Torre combines a GPU-accelerated FETD forward routine and a multigrid-based inversion approach, where the triangular mesh \mathcal{T} applied to discretise the permittivity distribution in the inversion stage is coarser than the one applied in the forward wave propagation. Each matrix \mathbf{L} was found by a GPU-accelerated deconvolution process. Using Dell 5820 Workstation equipped with 256 GB RAM and NVIDIA Quadro RTX 8000 GPU, the complete FETD simulation of the signals took approximately 8 and 30 minutes for a single point of the (A) 20 and (B) 60 MHz frequencies respectively and each \mathbf{L} was obtained in less than 10 seconds. The inversion mesh \mathcal{T} consisted of 896 triangles. The total variation regularisation parameters α was chosen experimentally to be 0.02 and 0.005 for the 20 and 60 MHz systems respectively, where $\beta = 0.01\alpha$ for both cases. In all, a total of 32 numerical experiments are considered as described in Table 2 given that two noise level cases are implemented in this study.

3. Results

The results from the numerical experiments of section 2.5 are presented in Figures 5–10. Of these, Figures 5 and 6 show the amplitude of the reconstructed real relative permittivity perturbation visualised on a logarithmic scale between -30 and 0 dB, with the highest amplitude scaled to zero. These also show the relative Overlap Error (OE) between the reconstructed details and those of the actual permittivity distribution. In Table 3, Figures 7 and 8, the robustness of the reconstructions are analysed in a tabular form and via boxplots obtained with 10 different noise vector realisations. The norm of the reconstructed permittivity distribution, \mathbf{x} , for the different sampling steps is shown for the randomised configuration and full data in Figure 10. Overall, the results show that the aim of reconstructing the permittivity of the complex domain was achieved by a monostatic full-wave simulation and inversion, with the formulation of a spatial and discrepancy-based frequency averaging method, compensating for the phase errors as formulated in this article.

3.1. Low vs. high centre frequency

The global structure of the two-dimensional test domain, including the surface layer and voids, was successfully reconstructed with both 20 and 60 MHz signals. The former gave the superior reconstruction outcome in terms of MSE and OE, while the latter with higher SSIM, shows faint details and hot spots on the surface. Especially in the concave part of the target leading to foci of intensive reflection and parts close to the receiver. This anomaly limits the visibility of the voids which is obvious based on their increased MSE and OE, as there is more contrast at the surface compared to the interior part. Moreover, the surface layer has a lesser OE, although not fully connected, hence leading to an increased MSE in comparison to the lower frequency case.

¹<https://github.com/sampsapursiainen/GPU-Torre>

3.2. Signal configuration

For the sparse configurations, the global structure, surface layer, and voids are generally more pronounced and uniform, with an enhanced contrast compared to the dense ones, which are of deteriorated reconstruction quality reflected by, for example, fluctuating artefacts and inconsistent intensity of the voids. Due to these anomalies, the MSEs and OEs of the dense (carrier-balanced) configurations are higher than those obtained for the sparse (bandwidth-balanced) ones. The difference between the results obtained with dense and sparse point density is less pronounced when the randomisation of the points and frequencies is applied. The randomised and frequency perturbed configurations have a smooth outcome compared to the cases of regular turn configurations, which result in a weaker visibility of the interior details and structure, as well as fractures within the voids and the surface layer. For the distinguishability of the details, the randomised configuration with sparse density is a preferable set-up, especially in the lower frequency case as shown in Figure 6. Noting that for the high frequency, based on the SSIM, MSE, and OE in Table 3, the global structure of the reconstructed domain is more conspicuous for the regular turn case, but not necessarily with respect to the void and surface layer.

3.3. Low vs. high noise

As expected, the reconstruction quality of the void was observed to be maximised with low noise (SNR 20 dB), while the higher noise level (SNR 12 dB) was observed to cause artefacts in the void. However, the latter allowed finding the interior details with a balance towards the surface. The characteristic difference between the low frequency and the high frequency configuration is maintained regardless of the noise level. The structure obtained with the latter remains smooth while the visibility of the void details weakens with higher noise. Similarly, the global structure with respect to SSIM suggests that the difference between the noise levels seems comparable in significance, to the difference between the configurations. The low noise level amplifies the visibility of the void with respect to the OE measure, but the MSE shows that higher noise level gives more visibility for the void and surface layer.

3.4. Nonfiltered vs. TSVD

The TSVD filter can be observed to preserve the main details of the reconstruction, in essence the global structure, while filtering out minor fluctuations. The effect of the TSVD filter is pronounced when there are noise or phase errors in the data, i.e., when the noise and/or frequency of the signal is high. The reconstructions found with TSVD are balanced towards the surface layer, which can be considered as a predominating structure with respect to the scattered energy, and, therefore, its contribution to the large singular values and vectors constituting the TSVD, is enhanced.

3.5. SSIM, MSE, and OE

The MSE and OE are two complementary measures with the objective of evaluating the quality of the reconstructed domain. The MSE shows the exact difference between two different distributions, while OE gives an idea of the localisation and contrast of the reconstructed details. The effect of the mathematical approach on the reconstruction can be observed as a deviation in MSE and OE. The results show that the MSE and OE give a similar pattern in evaluating the voids and

Table 3: Similarity and error estimates of the reconstructions for different numerical configurations. The 1st column presents the two signal pulses (A) 20 and (B) 60 MHz, described in Table 1, while the 2nd column shows several configurations over which these frequencies have been experimented. The corresponding levels of the configurations are also highlighted in the 3rd column. The 4th to 8th columns give the mean values with respect to the different centre frequencies, configurations, and levels for SSIM, void MSE, surface MSE, void OE, and surface OE. The WRS test values are also highlighted, with 0 implying no significant differences and 1 implying a significant difference in the median values of the corresponding distributions.

Signal pulse	Configu- ration	Levels	SSIM		MSE				OE %			
				WRS	Void	WRS	Surface	WRS	Void	WRS	Surface	WRS
(A) 20 MHz			0.530		2.074		1.602		58.387		38.868	
	Spatial averaging	Dense	0.527	1	2.286	1	1.725	1	60.476	1	40.741	1
		Sparse	0.533		1.863		1.480		56.298		36.995	
	Point selection	Regular	0.521	1	2.224	1	1.751	1	60.671	1	43.176	1
		Random	0.539		1.925		1.453		56.103		34.559	
	Filtering	None	0.530	0	2.060	0	1.603	0	58.389	0	38.435	0
		TSVD	0.530		2.088		1.602		58.384		39.301	
	Noise	Low	0.530	0	2.085	0	1.657	1	55.933	1	39.795	0
		High	0.530		2.064		1.548		60.840		37.940	
(B) 60 MHz			0.673		4.787		3.833		78.668		31.785	
	Spatial averaging	Dense	0.672	0	4.797	0	3.787	0	79.527	1	31.612	0
		Sparse	0.674		4.777		3.880		77.810		31.957	
	Point selection	Regular	0.680	0	4.840	1	3.957	1	80.045	1	33.058	1
		Random	0.667		4.735		3.708		77.292		30.511	
	Filtering	None	0.672	0	4.780	0	3.827	0	78.339	0	31.560	0
		TSVD	0.673		4.794		3.839		79.000		32.009	
	Noise	Low	0.710	1	4.855	1	4.094	1	76.195	1	33.483	1
		High	0.636		4.720		3.572		81.142		30.086	

the surface layer. The SSIM was further used as the evaluating criteria for the global structure of the reconstructed domain, complementing the noise effect in the interior structure.

The WRS test shows that the levels of the configurations are significantly different in the dense vs. sparse and regular vs. random for the 20 MHz case s shown in Table 3. Similarly, the MSE surface and OE void of the noise configuration also have significantly different medians for the low and high noise distributions. The TSVD vs. non-filtered levels are insignificant for all their corresponding measures. For the 60 MHz case, only the low vs. high noise distributions have significantly different medians for all their corresponding measures.

The correlation heatmap in Figure 9 shows that the SSIM has a strong negative correlation with other measures ranging from -0.97 with OE surface, -0.9 with MSE surface, -0.82 with

MSE void, and -0.72 with OE void for the 20 MHz case. This is expected since the highest SSIM values correspond to the lowest values of other measures and vice versa as shown in Table 3. Other measures are positively correlated between themselves with the highest being 0.96 between MSE surface and OE surface, and the least being 0.58 between OE void and MSE surface. In the 60 MHz case, OE void is also negatively correlated with other measures, the strongest being -0.74 with SSIM and the least being -0.33 with MSE void. The other measures have strong positive intermeasure correlations ranging from 0.98 between MSE void and OE surface to 0.87 between MSE void and SSIM.

3.6. Convergence

An investigation of the convergence and performance of several configurations on the full data is presented in Figure 10. The plots in Figure 10 all start from zero on a norm scale to indicate the variation of the magnitude for each configuration. The upper limits are however retained for clear visibility of the spread in the respective distribution. The uncertainty in the reconstructed estimates \mathbf{x} spreads on the norm scale as the noise increases for both 20 and 60 MHz frequencies. The dense configuration is of lower magnitude and spread compared to the sparse case, which also shows spurious outliers beyond the 5% to 95 % quantile range. The effect of the randomised frequency perturbation is less evident in the dense configuration, especially in the low frequency case. The magnitude of the norm in the high frequency case is greater and its spread extends frequently outside the interquartile range. Figure 10 also indicates the effectiveness of the sampling process. Since the sample realisations are computationally demanding to obtain, the discrepancy conditions and averaging are selected such that the randomness in the process are present and the IID assumption holds.

4. Discussion

This article describes and evaluates numerically a filtering approach, which allows marginalising wavelength-induced random errors from a large full-waveform dataset. This approach enables obtaining a reconstruction of the surface layer and voids of a 160 m diameter non-convex two-dimensional asteroid model, via a monostatic measurement of a full-wavefield signal, having centre frequencies of 20 and 60 MHz and bandwidths of 10 and 20 MHz, respectively. Finding a reconstruction was feasible with 20 and 12 dB SNR, of which the former has been estimated as the lower bound of the CONSERT measurement of [8] and the latter is slightly (2 dB) above the 10 dB limit which has been suggested as the lower bound for finding a reasonable reconstruction for the interior structure of an asteroid model in the recent numerical simulations and laboratory experiments [37, 34, 13, 18, 14].

We demonstrate through numerical experiments that, when a centre frequency applicable in a space mission is used in the numerical simulation of the full-wavefield, i.e., 20 MHz of the DISCUS concept [9] or 60 MHz of JuRa [11], together with quadrature amplitude modulation and demodulation of the simulated signal [18], the reconstruction will be corrupted by phase errors, if the wavefield is not averaged over spatial points or filtered by decomposing the signal into meaningful and noisy parts. The present results show that the expected effect of phase errors is of significantly higher magnitude in comparison to the noise level, and that this effect can be

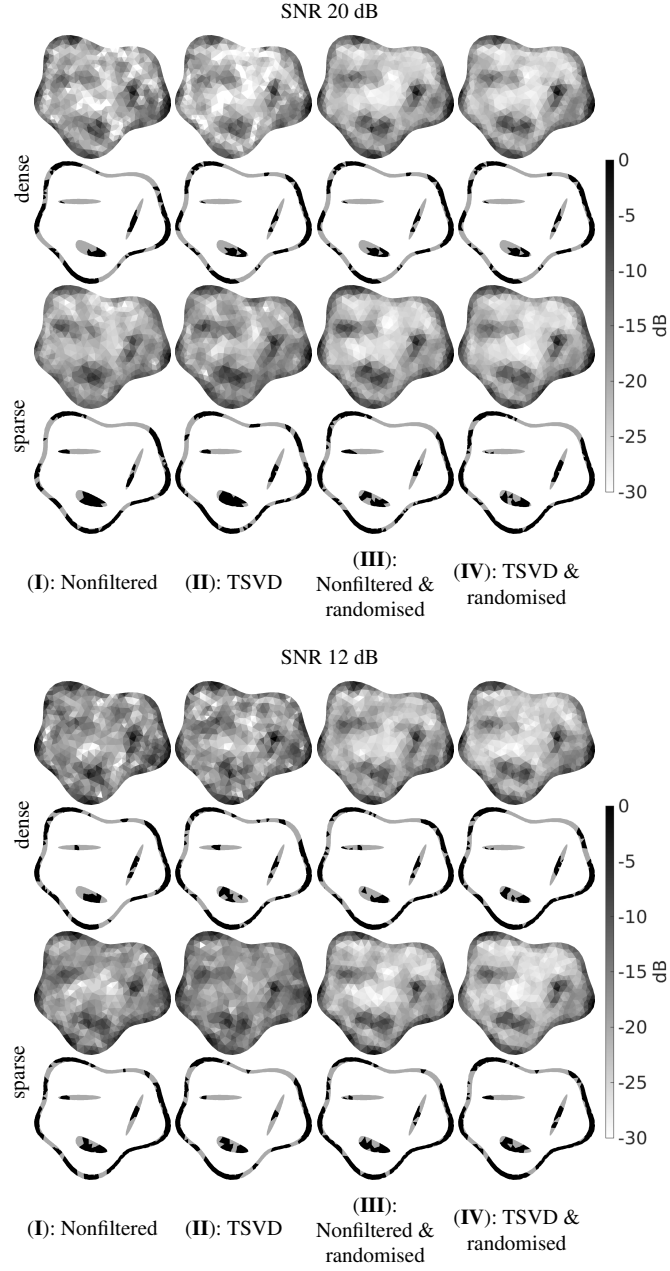


Figure 5: Examples of individual permittivity reconstructions obtained using the 20 MHz signal pulse (A) with SNR of 20 dB (1st–4th row) and 12 dB (5th–8th row), and their corresponding overlap reconstruction showing how much surface and void details are reconstructed. The odd rows show the permittivity reconstructions and the even rows show the overlap reconstructions. The top row shows the results for the dense carrier-balanced configuration with 64 points and the bottom row for the sparse bandwidth-balanced one with 32 points. The results for configurations (I)–(IV) are shown in columns from left to right, respectively.

reduced via spatial and frequency-based sampling, i.e., averaging over a higher number of points in the spatial and spectral domains, consequently, improving the reconstruction. This is evident

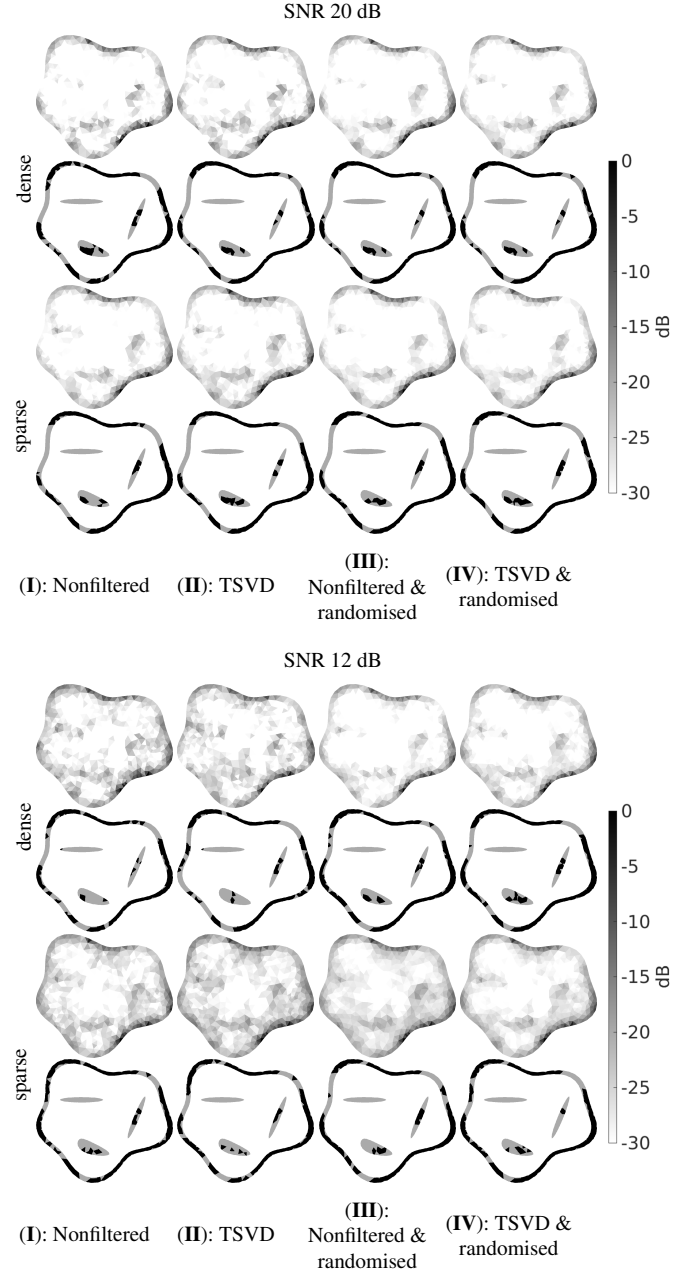


Figure 6: Examples of individual permittivity reconstructions obtained using the 60 MHz signal pulse (**B**) with SNR of 20 dB (1st–4th row) and 12 dB (5th–8th row), and their corresponding overlap reconstruction showing how much surface and void details are reconstructed. The odd rows show the permittivity reconstructions and the even rows show the overlap reconstructions.. The top row shows the results for the dense carrier-balanced configuration with 128 points and the bottom row for the sparse bandwidth-balanced one with 64 points. The results for configurations **(I)**–**(IV)** are shown in columns from left to right, respectively.

in the comparison of results for dense and sparse sets where the phase errors can be identified as the cause of the difference in the reconstruction obtained. The significance of the results is

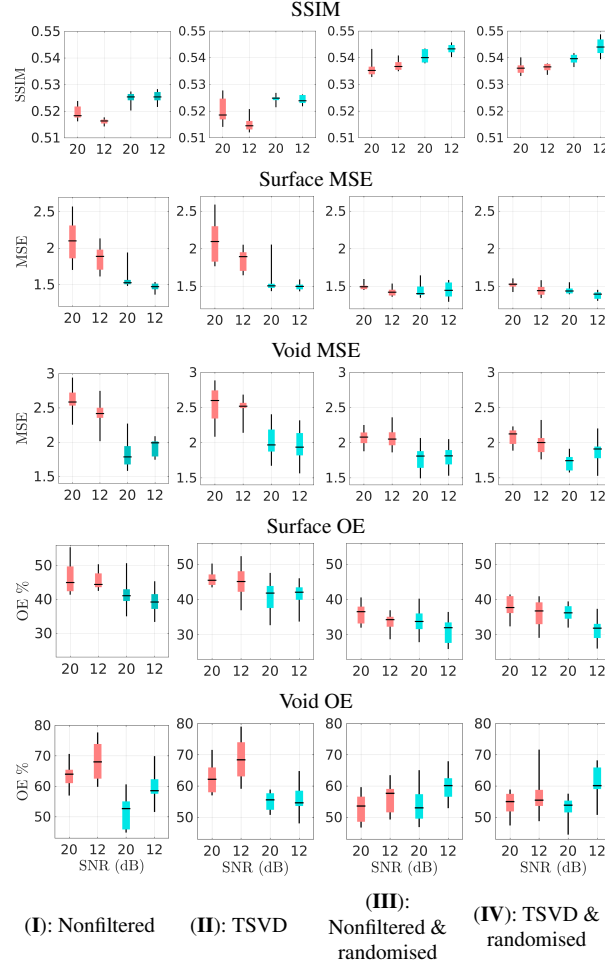


Figure 7: Structural Similarity (SSIM, scale of 0 - 1 and 1 shows the best result), Mean Squared Error (MSE, lower limit of 0, which shows the best result) and Overlap Error (OE %, scale of 0 - 100 and 0 shows the best result) for the 20 MHz signal pulse (A) with SNR of 20 and 12 dB.

highlighted if the global internal structure of an asteroid is to be explored during a space mission, to provide answers to the important planetary scientific questions on asteroids and/or comets and their internal composition [38, 39, 40].

The assumption of independent and identically distributed (IID) total variation regularised estimates sets a challenge for choosing the measurement point configuration and phase discrepancy appropriately. We covered two possible strategies for spatial point selection, otherwise known as statistical sparsity-based learning with a suitable prior model [41]. The sample size of the present randomised configuration was found to reduce the phase-dependent fluctuations significantly. Further improvement of the current estimates might be obtained by applying a larger sample, relying on the asymptotic central limit theorem, which states that the accuracy of a sample-based estimate is inversely proportional to the square root of the sample size. Alternatively, as the IID condition is only assumed due to the missing *a priori* information on the phase errors, the formation of the sample can be supervised by filtering out the possible outliers. In such a procedure, the principal

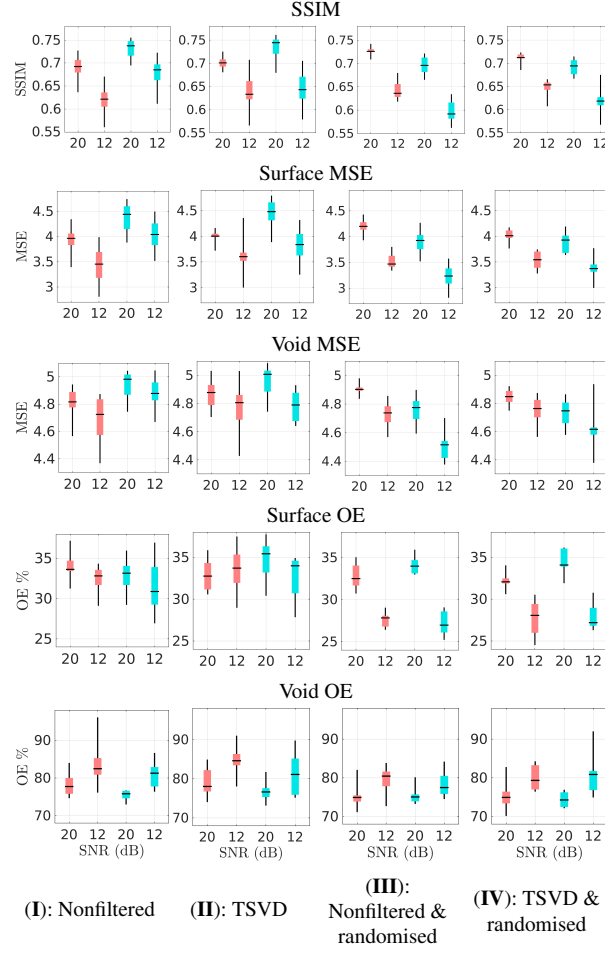


Figure 8: Structural Similarity (SSIM, scale of 0 - 1 and 1 shows the best result), Mean Squared Error (MSE, lower limit of 0, which shows the best result) and Overlap Error (OE %, scale of 0 - 100 and 0 shows the best result) for the 60 MHz signal pulse (B) with SNR of 20 and 12 dB.

component analysis [42], or machine learning and deep neural network [43, 44] might be utilised.

From a potential mission design viewpoint, the results obtained suggest that setting the bandwidth of the modelled signal pulse based on the discrepancy principle, and averaging the measurement point density following the Nyquist criterion is crucial w.r.t. stability of the reconstruction process. If the number of averaging points is limited further from the current setup, the size of the reconstructed details grows or they tend to get blurred as a natural consequence of the lower measurement point density. Due to the importance of selecting the measurement point configuration suggested by the WRS test, it is also obvious that a sparse bandwidth-based configuration alone will not allow obtaining an optimal reconstruction quality. However, sampling can be applied without having a point density matching with the Nyquist criterion for the centre frequency, which can be the case of *in-situ* measurements.

The TSVD filter is based on excluding the less significant signal components out of the inversion process, which is known to improve the outcome of GPR reconstructions [30]. As shown by the WRS test, TSVD was found to have a regularising effect on the reconstruction, while it

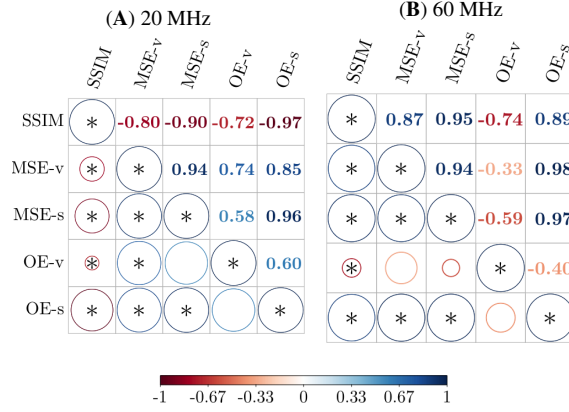


Figure 9: Correlation heatmap between structural similarity (SSIM), Mean Squared Error void (MSE-v), Mean Squared Error surface (MSE-s), Overlap Error void (OE-v) and Overlap Error surface (OE-s) with respect to the mean values in Table 3. The significant correlation are shown with the asterisk sign *, the insignificant correlation are depicted with no asterisk at a 5% significance level. The size of the circle shows the magnitude of significance and insignificance; larger circle implying high significance or insignificance. The colour shows the magnitude of the correlation for both centre frequencies (A) 20 and (B) 60 MHz, configurations.

did not affect the major fluctuations due to the phase errors which could only be appropriately resolved via the statistical approach. As our concentration is on the monostatic data, i.e., the points of transmission and measurement coincide, similar to the future JuRa investigation, TSVD can be considered as an efficient way to decompose the signal. If more complex signal patterns, e.g., bistatic or multistatic measurements, will need to be processed, as suggested in several previous studies [34], then more advanced decomposition approaches will be necessary, for example, the decomposition of the time reversal operator DORT (Décomposition de l'opérateur de retournement temporel) [45, 46], which finds the most 'reflective' multistatic patterns by finding the eigenvalues and eigenvectors of a symmetric (reciprocal) transfer matrix between the transmission and measurement points.

While our concentration is on reconstructing the real part of the relative permittivity structure, which would allow a real formulation of the forward model and the inverse procedure, see, e.g., [17], a complex formulation has been applied. This was found to be advantageous to reduce any possible fluctuations due to phase errors. Namely, a phase error might affect only one of the QAM signal components, in which case, a real Jacobian matrix might contain two opposite fluctuations, potentially cancelling each other, while a complex Jacobian takes both perturbations appropriately into account as two complex components with a positive absolute value, thereby, preserving the visibility of the scatterer causing the deviation.

The full-wavefield inversion process applied relies on the first-order Born approximation, i.e., the linearization of the wavefield w.r.t. the permittivity perturbation in a given position. Hence, while the wave propagation is modelled as a non-linear process, taking into account indirect signal paths including reflection and refraction, some higher-order scattering effects, e.g., the coupling effects between the scattering obstacles, are omitted in this study. Based on earlier results of the same model, the improvement obtained with a higher-order Born approximation via a recursive use of the present linearization [17] is assumed to be a minor one. Notably, the numerical inaccuracies

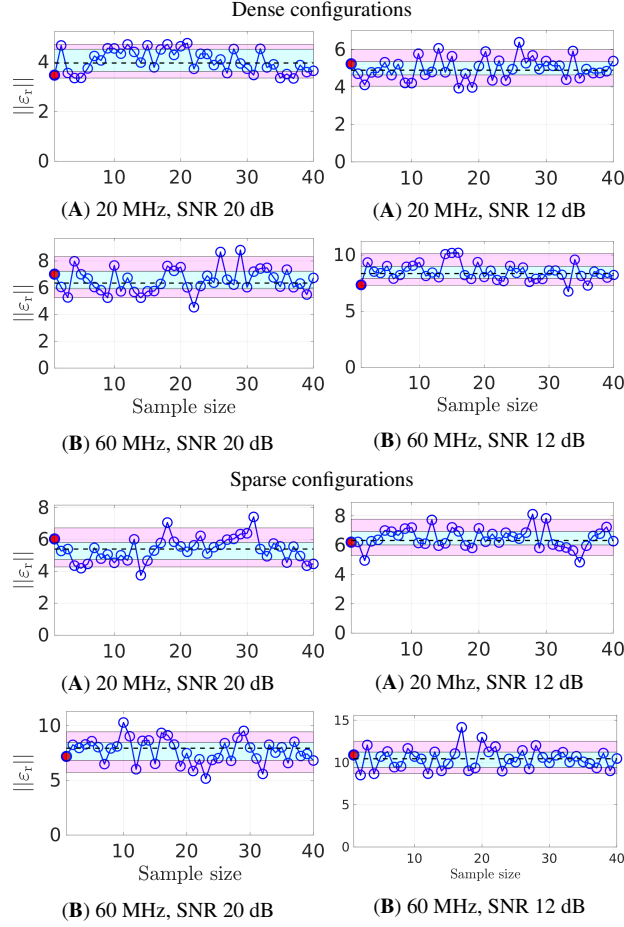


Figure 10: The average absolute value for the entries of \mathbf{x} as a function of the different sampling steps in the case of the nonfiltered & randomised data. The 1st and 2nd row show the results for the dense configuration, while the 3rd and 4th row indicates the sparse configuration. The red marker indicates an update in the centre frequency applied in the signal demodulation process. The purple area shows the range from 5 to 95 % quantile of the sample variation, the cyan area shows 25 to 50 % quantile, and the dashed line shows the median of the samples. The magnitude of \mathbf{x} can be observed to grow as the noise, signal frequency, and sparsity of the measurement point configuration grows.

in the modelled material distribution, which gives rise to the requirement for the discrepancy condition, are always present regardless of the order of Born approximation incorporated in the model. However, another modelling approach for the higher-order scattering effects might yield an improvement. Therefore, comparisons between different methods and solvers, e.g., ray-tracing techniques [47, 48] and frequency based methods [49, 13] will be important.

We have chosen a two-dimensional reference domain for this study, as it allows examining the effect of the phase errors on numerical full-wavefield inversion efficiently without the need of high performance cluster computations. The next step will be to investigate the present methodology with a three-dimensional analogue object and with experimental scattering data similar to [18, 50, 13]. In such a process, the outcome of this study to understand combining point cloud data into a single reconstruction is important. The current two-dimensional implementation can,

in principle, be directly extended to the three-dimensional laboratory coordinates as done in the previous analogue studies. This study also allows for further numerical investigation of the uncertainties relating to the carrier-induced effects, which is essential due to the significance of their magnitude based on the current results and, e.g., the recent findings presented in [14]. In particular, a deeper investigation on the dependence of the phase errors on the frequency and position might be conducted to gain more *a priori* understanding about how they might be distributed.

References

- [1] W. C. Chew, Y.-M. Wang, Reconstruction of two-dimensional permittivity distribution using the distorted born iterative method, *IEEE transactions on medical imaging* 9 (1990) 218–225.
- [2] S. Carlsten, S. Johansson, A. Wörman, Radar techniques for indicating internal erosion in embankment dams, *Journal of applied geophysics* 33 (1995) 143–156.
- [3] S. Y. Semenov, A. E. Bulyshev, A. Abubakar, V. G. Posukh, Y. E. Sizov, A. E. Souvorov, P. M. Van Den Berg, T. C. Williams, Microwave-tomographic imaging of the high dielectric-contrast objects using different image-reconstruction approaches, *IEEE transactions on Microwave Theory and Techniques* 53 (2005) 2284–2294.
- [4] J. R. Ernst, A. G. Green, H. Maurer, K. Holliger, Application of a new 2d time-domain full-waveform inversion scheme to crosshole radar data, *Geophysics* 72 (2007) J53–J64.
- [5] S. Pursiainen, M. Kaasalainen, Orbiter-to-orbiter tomography: a potential approach for small solar system bodies, *IEEE Transactions on Aerospace and Electronic Systems* 52 (2016) 2747–2759.
- [6] J. Wiskin, B. Malik, D. Borup, N. Pirshafiey, J. Klock, Full wave 3d inverse scattering transmission ultrasound tomography in the presence of high contrast, *Scientific Reports* 10 (2020) 1–14.
- [7] W. Kofman, A. Herique, J.-P. Goutail, T. Hagfors, I. Williams, E. Nielsen, J.-P. Barriot, Y. Barbin, C. Elachi, P. Edenhofer, A.-C. Levasseur-Regourd, D. Plettemeier, G. Picardi, R. Seu, V. Svedhem, The comet nucleus sounding experiment by radiowave transmission (consert): A short description of the instrument and of the commissioning stages., *Space Science REviews* 128 (2007).
- [8] W. Kofman, A. Herique, Y. Barbin, J.-P. Barriot, V. Ciarletti, S. Clifford, P. Edenhofer, C. Elachi, C. Eyraud, J.-P. Goutail, E. Heggy, L. Jorda, J. Lasue, A.-C. Levasseur-Regourd, E. Nielsen, P. Pasquero, F. Preusker, P. Puget, D. Plettemeier, Y. Rogez, H. Sierks, C. Statz, H. Svedhem, I. Williams, S. Zine, J. Van Zyl, Properties of the 67p/churyumov-gerasimenko interior revealed by consort radar, *Science* 349 (2015) aab0639–1 – aab0639–6.
- [9] P. Bambach, J. Deller, E. Vilenius, S. Pursiainen, M. Takala, H. M. Braun, H. Lentz, M. Wittig, Discuss—the deep interior scanning cubesat mission to a rubble pile near-earth asteroid, *Advances in Space Research* 62 (2018) 3357–3368.
- [10] CDF, Study report, in: SPP NEO Inactive Body, volume CDF–A(178), January, 2018, pp. 15–19.
- [11] A. Herique, D. Plettemeier, H. Goldberg, W. Kofman, Jura: the juvenas radar on hera to fathom didymoon, in: *European Planetary Science Congress, 2020*, pp. EPSC2020–595.
- [12] A. Herique, D. Plettemeier, W. Kofman, Y. Rogez, H. Goldberg, Low frequency radar (lfr) on the juvenas cubesat for hera/esa mission, in: *EGU General Assembly Conference Abstracts, 2020*, p. 19957.
- [13] C. Eyraud, L.-I. Sorsa, J.-M. Geffrin, M. Takala, G. Henry, S. Pursiainen, Full wavefield simulation versus measurement of microwave scattering by a complex 3d-printed asteroid analogue, *Astronomy & Astrophysics* 643 (2020) A68.
- [14] J. Deng, W. Kofman, P. Zhu, A. Hérique, R. Liu, S. Zheng, Ei+ fwi method for reconstructing interior structure of asteroid using lander-to-orbiter bistatic radar system, *IEEE Transactions on Geoscience and Remote Sensing* (2021).
- [15] M. Takala, D. Us, S. Pursiainen, Multigrid-based inversion for volumetric radar imaging with asteroid interior reconstruction as a potential application, *IEEE Transactions on Computational Imaging* 4 (2018) 228–240.
- [16] L. Van Hove, Correlations in space and time and born approximation scattering in systems of interacting particles, *Physical Review* 95 (1954) 249.
- [17] L.-I. Sorsa, M. Takala, C. Eyraud, S. Pursiainen, A time-domain multigrid solver with higher-order born ap-

- proximation for full-wave radar tomography of a complex-shaped target, *IEEE Transactions on Computational Imaging* 6 (2020) 579–590.
- [18] L.-I. Sorsa, S. Pursiainen, C. Eyraud, Analysis of full microwave propagation and backpropagation for a complex asteroid analogue via single-point quasi-monostatic data, *Astronomy & Astrophysics* 645 (2021) A73. doi:[10.1051/0004-6361/202039380](https://doi.org/10.1051/0004-6361/202039380).
 - [19] D. J. Daniels, *Ground penetrating radar*, volume 1, Iet, 2004.
 - [20] M. Bousquet, *Satellite Communications and Space Telecommunication Frequencies*, Springer International Publishing, Cham, 2017, pp. 325–357. doi:[10.1007/978-3-319-23386-4_13](https://doi.org/10.1007/978-3-319-23386-4_13).
 - [21] S. J. Orfanidis, *Introduction to signal processing*, Prentice-Hall, Inc., 1995.
 - [22] K. Egiazarian, A. Foi, V. Katkovnik, Compressed sensing image reconstruction via recursive spatially adaptive filtering, in: *2007 IEEE International Conference on Image Processing*, volume 1, IEEE, 2007, pp. I–549.
 - [23] B. Finetti, *Probability, induction and statistics*, John Wiley and Sons, 1972.
 - [24] J. S. Liu, *Monte Carlo strategies in scientific computing*, Springer Science & Business Media, 2008.
 - [25] O. Bucci, G. Franceschetti, On the spatial bandwidth of scattered fields, *IEEE Trans. Antennas Propag* 35 (1987).
 - [26] F. Luisier, P. Rodríguez, Total variation regularization algorithms for images corrupted with different noise models: A review, *Journal of Electrical and Computer Engineering* 2013 (2013) 217021. URL: <https://doi.org/10.1155/2013/217021>. doi:[10.1155/2013/217021](https://doi.org/10.1155/2013/217021).
 - [27] E. J. Candes, J. K. Romberg, T. Tao, Stable signal recovery from incomplete and inaccurate measurements, *Communications on Pure and Applied Mathematics: A Journal Issued by the Courant Institute of Mathematical Sciences* 59 (2006) 1207–1223.
 - [28] E. J. Candès, J. Romberg, T. Tao, Robust uncertainty principles: Exact signal reconstruction from highly incomplete frequency information, *IEEE Transactions on information theory* 52 (2006) 489–509.
 - [29] G. H. Golub, C. F. Van Loan, *Matrix computations*, volume 3, JHU press, 2013.
 - [30] G. Ludeno, G. Gennarelli, S. Lambot, F. Soldovieri, I. Catapano, A comparison of linear inverse scattering models for contactless gpr imaging, *IEEE Transactions on Geoscience and Remote Sensing* 58 (2020) 7305–7316.
 - [31] W. Kofman, Radar techniques to study subsurfaces and interiors of the solar system objects, in: *2012 19th International Conference on Microwaves, Radar Wireless Communications*, volume 2, 2012, pp. 409–412. doi:[10.1109/MIKON.2012.6233605](https://doi.org/10.1109/MIKON.2012.6233605).
 - [32] A. Hérique, D. Plettemeier, W. Kofman, Y. Rogez, C. Buck, H. Goldberg, A low frequency radar to fathom asteroids from juvenas cubesat on hera, in: *Proc. EPSC-DPS Joint Meeting*, volume 13, EPSC-DPS Joint Meeting 2019, Geneva, Switzerland, 2019, p. 807.
 - [33] R. P. Binzel, W. Kofman, Internal structure of near-earth objects, *Comptes Rendus Physique* 6 (2005) 321–326.
 - [34] L.-I. Sorsa, M. Takala, P. Bambach, J. Deller, E. Vilenius, S. Pursiainen, Bistatic full-wave radar tomography detects deep interior voids, cracks and boulders in a rubble-pile asteroid model, *The Astrophysical Journal* 872(1):44 (2019).
 - [35] Z. Wang, A. C. Bovik, H. R. Sheikh, E. P. Simoncelli, Image quality assessment: from error visibility to structural similarity, *IEEE transactions on image processing* 13 (2004) 600–612.
 - [36] J. D. Gibbons, S. Chakraborti, *Nonparametric statistical inference: revised and expanded*, CRC press, 2014.
 - [37] M. Takala, P. Bambach, J. Deller, E. Vilenius, M. Wittig, H. Lentz, H. Braun, M. Kaasalainen, S. Pursiainen, Far-field inversion for the deep interior scanning cubesat, *IEEE Transactions on Aerospace and Electronic Systems* (2018).
 - [38] B. Carry, Density of asteroids, *Planetary and Space Science* 73 (2012) 98–118.
 - [39] M. Jutzi, W. Benz, Formation of bi-lobed shapes by sub-catastrophic collisions—a late origin of comet 67p’s structure, *Astronomy & Astrophysics* 597 (2017) A62.
 - [40] A. Hérique, B. Agnus, E. Asphaug, A. Barucci, P. Beck, J. Bellerose, J. Biele, L. Bonal, P. Bousquet, L. Bruzzone, C. Buck, I. Carnelli, A. Cheng, V. Ciarletti, M. Delbo, J. Du, X. Du, C. Eyraud, W. Fa, J. G. Fernandez], O. Gassot, R. Granados-Alfaro, S. Green, B. Grieger, J. Grundmann, J. Grygorczuk, R. Hahnel, E. Heggy, T.-M. Ho, O. Karatekin, Y. Kasaba, T. Kobayashi, W. Kofman, C. Krause, A. Kumamoto, M. Küppers, M. Laabs, C. Lange, J. Lasue, A. Lévassieur-Regourd, A. Mallet, P. Michel, S. Mottola, N. Murdoch, M. Mütze, J. Oberst,

- R. Orosei, D. Plettemeier, S. Rochat, R. RodriguezSuquet, Y. Rogez, P. Schaffer, C. Snodgrass, J.-C. Souyris, M. Tokarz, S. Ulamec, J.-E. Wahlund, S. Zine, Direct observations of asteroid interior and regolith structure: Science measurement requirements, *Advances in Space Research* 62 (2018) 2141–2162.
- [41] A. Mirbeik, V. Lawrence, T. A. LaPeruta, C. M. Popescu, M. E. Hohil, N. Tavassolian, Statistical sparsity-based learning for ultra-wideband radar signal reconstruction, in: *Artificial Intelligence and Machine Learning for Multi-Domain Operations Applications III*, volume 11746, International Society for Optics and Photonics, 2021, p. 1174619.
- [42] K.-C. Lee, J.-S. Ou, M.-C. Fang, Application of svd noise-reduction technique to pca based radar target recognition, *Progress In Electromagnetics Research* 81 (2008) 447–459.
- [43] P. Lang, X. Fu, M. Martorella, J. Dong, R. Qin, X. Meng, M. Xie, A comprehensive survey of machine learning applied to radar signal processing, *arXiv preprint arXiv:2009.13702* (2020).
- [44] Y. Ji, F. Zhang, J. Wang, Z. Wang, P. Jiang, H. Liu, Q. Sui, Deep neural network-based permittivity inversions for ground penetrating radar data, *IEEE Sensors Journal* 21 (2021) 8172–8183.
- [45] C. Prada, S. Manneville, D. Spoliansky, M. Fink, Decomposition of the time reversal operator: Detection and selective focusing on two scatterers, *The Journal of the Acoustical Society of America* 99 (1996) 2067–2076.
- [46] M. Fink, D. Cassereau, A. Derode, C. Prada, P. Roux, M. Tanter, J.-L. Thomas, F. Wu, Time-reversed acoustics, *Reports on progress in Physics* 63 (2000) 1933.
- [47] O. Gassot, A. Hérique, Y. Rogez, W. Kofman, S. Zine, P.-P. Ludimbulu, Sprats: a versatile simulation and processing radar tools for planetary missions, in: *2020 IEEE Radar Conference (RadarConf20)*, IEEE, 2020, pp. 1–5.
- [48] Ciarletti, V., Levasseur-Regourd, A. C., Lasue, J., Statz, C., Plettemeier, D., Hérique, A., Rogez, Y., Kofman, W., CONSERT suggests a change in local properties of 67P/Churyumov-Gerasimenko’s nucleus at depth, *A&A* 583 (2015) A40. URL: <https://doi.org/10.1051/0004-6361/201526337>. doi:10.1051/0004-6361/201526337.
- [49] C. Eyraud, H. Saleh, J.-M. Geffrin, Influence of the description of the scattering matrix on permittivity reconstruction with a quantitative imaging procedure: polarization effects, *JOSA A* 36 (2019) 234 – 244.
- [50] L.-I. Sorsa, C. Eyraud, A. Hérique, M. Takala, S. Pursiainen, J.-M. Geffrin, Complex-structured 3d-printed wireframes as asteroid analogues for tomographic microwave radar measurements, *Materials & Design* 198 (2021) 109364. doi:<https://doi.org/10.1016/j.matdes.2020.109364>.

Acknowledgement

This study was carried out through the Academy of Finland project, ICT 2023 (FETD-Based Tomographic Full-Wave Radar Imaging of Small Solar System Body Interiors; project number 336151), and was supported by the Academy of Finland Centre of Excellence in Inverse Modelling and Imaging, 2018-2025.